electrochem

MDPI

Article

Anodic Thin Films on Gadolinium, Al/Gd and Al/Nb/Gd Systems: Morphology, Growth Mechanisms and Niobia Cork-like Effect

Andrei Pligovka [1,*], Sergey Zavadski [2], Andrei Lazavenka [3] and Vadim Bogush [4]

[1] Research and Development Laboratory 4.10 "Nanotechnologies", Belarusian State University of Informatics and Radioelectronics, 6 P. Brovki Street, 220013 Minsk, Belarus
[2] Centre 2.1 "Plasma Processing Research Center", Belarusian State University of Informatics and Radioelectronics, 6 P. Brovki Street, 220013 Minsk, Belarus; szavad@bsuir.by
[3] Independent Researcher, 02-740 Warsaw, Poland; lozovenko.andrey@gmail.com
[4] Belarusian State University of Informatics and Radioelectronics, 6 P. Brovki Street, 220013 Minsk, Belarus; bogush@bsuir.by
* Correspondence: pligovka@bsuir.by; Tel.: +375-44-730-95-81; Fax: +375-17-293-23-56

Abstract

The high reactivity of lanthanide metals poses a challenge to the electrochemical anodizing of surfaces for nanostructured coatings. This paper presents the first systematic experimental investigation of anodic oxidation of lanthanide gadolinium in aqueous solutions of citric, boric, oxalic, and tartaric acids. The voltage-current-time responses of anodizing of gadolinium, Al/Gd and Al/Nb/Gd systems were investigated. Anodic thin films were characterized using modern analysis techniques: SEM, FIB, and EDX. Morphology and voltage-current-time response analysis of anodized Al/Nb/Gd systems made it possible to establish the niobia cork-like effect and to develop a growth model.

Keywords: aluminum oxide; anodization; Gd_2O_3; Nb_2O_5; niobium oxide; valve metal; rare earth metals; magnetic materials; $GdNbO_4$; Al_2O_3

Check for updates

Academic Editor: Urszula Lelek-Borkowska

Received: 24 December 2025
Revised: 8 February 2026
Accepted: 14 February 2026
Published: 20 February 2026

Copyright: © 2026 by the authors. Licensee MDPI, Basel, Switzerland. This article is an open access article distributed under the terms and conditions of the Creative Commons Attribution (CC BY) license.

1. Introduction

Gadolinium is a rare earth metal of the lanthanide series discovered in 1880 [1]. It exhibits moderate chemical activity in air and water than most lanthanides, a property linked to its stable, half-filled $4f^7$ electron configuration ([Xe] $4f^7$ $5d^1$ $6s^2$). This configuration confers unique properties, most notably the highest magnetic moment among the elements. However, in terms of chemical activity, a fully filled f shell (as in lutetium, Lu) confers even greater stability than a half-filled one (Gd) [2–7].

The moderate chemical activity of gadolinium, relative to other lanthanides, makes it a promising candidate for forming nanostructured oxides via electrochemical anodizing. Gadolinium oxides, primarily Gd_2O_3, possess unique properties that enable specialized high-tech applications. In nuclear technology, Gd_2O_3-based ceramics or composites (e.g., with Cr_2O_3) are used in control rods to absorb neutrons and regulate chain reactions [6,8,9]. As a radiation shield, adding Gd_2O_3 to concrete or glass enhances neutron absorption, critical for protecting personnel at nuclear facilities [10,11]. In neutron optics, it serves as a component in collimators and filters for non-destructive testing [12]. In electronics and photonics, its wide band gap (~5.4 eV) makes it an excellent dielectric and insulator [13–15], while its high refractive index is valuable for optical applications [16,17].

Gd^{3+} ions are effective luminescence activators for other ions [18,19] and are themselves emitters in the UV range. Gd_2O_3 acts as both a host matrix and an activator for phosphors [20–22]. A prominent example is Gd_2O_2S:Pr (gadolinium oxysulfide doped with praseodymium), one of the most efficient phosphors for X-ray detectors in medical and industrial computed tomography and digital radiography, due to its high efficiency in converting X-rays to visible light [23,24]. Similarly, Eu^{3+}-doped gadolinium oxide (Gd_2O_3:Eu^{3+}) produces intense red luminescence, which is utilized in displays and fluorescent lamps [25–27].

Gd_2O_3-based ceramics are key materials for scintillators, which emit light upon absorbing ionizing radiation and are employed in particle detectors and medical imaging [28,29]. Furthermore, incorporating Gd_2O_3 into specialty glasses enhances their refractive index and radiation resistance (reducing darkening), making them suitable for high-precision optics and laser technologies [30–33].

Owing to its high melting point and resistance to degradation [34,35], Gd_2O_3 is employed as a catalyst or promoter in high-temperature chemical processes, including oil cracking, hydrogenation, and polymer synthesis [36–45]. It is also a key component in advanced ceramics, where it enhances thermal and mechanical properties [46,47].

Gd^{3+} ions possesses a strong paramagnetic moment. While chelate complexes of gadolinium are the current clinical standard for MRI contrast agents, Gd_2O_3-based nanoparticles are under active investigation as a next-generation alternative, offering the potential for higher efficacy and improved safety [48–51].

Conventional methods for synthesizing Gd_2O_3 nanostructures—including coprecipitation [52,53], sol–gel processing [54,55], hydro-/solvothermal synthesis [56–58], laser ablation [59,60] and PVD [61]—are typically classified as either chemical or physical. These techniques are often complex, require expensive equipment and precursors, and can lack precise control over the nanostructure arrays. In contrast, electrochemical anodizing of metallic gadolinium thin films through porous anodic alumina templates represents a promising alternative route. This approach has the potential to be a simpler, more cost-effective, and better-controlled method for producing ordered arrays of nanostructures with tunable and reproducible characteristics.

The first barrier anodizing of gadolinium was reported in 1982 by Nishikawa and Minami, using solutions of 0.01 M Na_2HPO_4–5% H_2O–ethylene glycol and 0.01 M KOH–5% H_2O–ethylene glycol [62]. In a separate study, a gadolinium rod was anodized in a 0.1 M sodium metasilicate solution (0.1 M $Na_2SiO_3 \cdot 9H_2O$) and the composition of the resulting film was analyzed [63]. Later, ultrathin anodic gadolinium oxide films were proposed [64] and subsequently investigated as promising *high-κ* gate dielectrics [65].

Nanostructured valve metal oxides formed by electrochemical anodizing have opened up possibilities for their potential application in thin-film capacitors [66], dental materials [67] and semiconductor devices [68]. The production of nanostructured gadolinium oxides by electrochemical anodizing will also expand its application areas and reduce material consumption.

In this work, Gd, Al/Gd and Al/Nb/Gd systems were prepared using a gadolinium scrap and thin film magnetron sputtering. These systems in aqueous solutions of citric, boric, oxalic and tartaric acids were anodized. Voltage-current-time responses, morphology and composition were investigated. This study establishes a foundation for the electrochemical nanostructuring of lanthanides through two distinct routes: anodizing via porous anodic alumina templates and anodizing assisted by an ultrathin valve-metal interlayer, exemplified here by niobium.

2. Materials and Methods

2.1. Preparation of Gadolinium Scrap, Aluminum and Niobium Thin Films

Experimental samples were prepared from pure gadolinium scrap (99.9%). The gadolinium scrap pieces measured 10 × 20 × 1 mm^3. Their surfaces were carefully prepared by sequential mechanical polishing on both sides: initial grinding with sandpaper (Klingspor Sp. z o.o., Bielsko-Biała, Poland) of increasing grit size (P40, P240, P320, P1000, and P2000, following ANSI standard) followed by final polishing with GOI paste (Polihimmed, Minsk, Belarus) on a felt wheel. The resulting surface quality corresponded to cleanliness class 8–10. Notably, even polishing up to P320 grit yielded a surface adequate for reproducible barrier anodizing. For magnetron sputtering, a more meticulous preparation was required. After each mechanical treatment, the samples were thoroughly rinsed with distilled water and dried under a stream of warm air.

The gadolinium scrap was used two or three times, first being re-ground and polished according to the method described above. The thickness of such samples decreased, depending on the number of uses, to 0.7–0.3 mm. It is assumed that the composition and properties of the samples did not change in this case.

After mechanical polishing, the exposure time of the gadolinium scrap to air was minimized and it was transferred to the deposition chamber without any intentional delay. All sputter depositions were performed under high-vacuum conditions, which effectively limited further surface oxidation prior to thin-film deposition.

Aluminum 1 μm and bilayer Al/Nb (1000/30 nm) were deposited by sputtering of 99.995% Al and 99.95% Nb targets, using a DC magnetron and ion beam method, respectively, on mechanically processed gadolinium scrap. The aluminum thickness was chosen based on considerations of sufficiency and cost effectiveness. Previous experimental experience of the authors and investigations [69,70] shows that when anodizing aluminum at a thickness significantly less than 1 μm, the anodic alumina formed has a non-uniform thickness, defects, and distorted pore geometry. At the same time, increasing the aluminum thickness beyond 1 μm has no effect on the quality of the anodic alumina, but it requires more time for sputtering and anodizing. Regarding the niobium thickness, the vacuum equipment at Center 2.1 allowed for the production of a continuous, reproducible, defect-free niobium film at a thickness of at least 30 nm. With the increasing thickness, a risk that the anodizing front would not reach the gadolinium or would reach it arises, but the effect would be insignificant.

Ion cleaning of the gadolinium scrap surface before deposition of aluminum and niobium for 600 s was carried out. The current and voltage of ion cleaning were 50 mA and 2500 V, respectively.

The deposition chamber was initially evacuated to 10^{-3} Pa, with subsequent sputtering using 99.998% argon at $2 \cdot 10^{-2}$ Pa for ion cleaning and ion beam sputtering, $6 \cdot 10^{-2}$ Pa for DC magnetron sputtering.

For DC magnetron method in the mode of discharge power stabilization, the discharge power was maintained at a level of 1 kW. In this case, the discharge voltage was 320 V.

For ion beam method in the mode of discharge power stabilization, the discharge power was maintained at a level of 150 mA. In this case, the discharge voltage was 4500 V.

2.2. Anodizing of Gadolinium Scrap, Al/Gd and Al/Nb/Gd Systems

Barrier anodizing of gadolinium and niobium was conducted in either a 1 wt.% aqueous citric acid solution and a 0.5 M boric acid solution with 0.05 M sodium tetraborate added to improve ion mobility. These electrolytes were selected due to their well-established use for valve-metal anodizing [66,71–73], including the oxidation of sublayers through porous alumina, as well as their low cost, ease of preparation, and long shelf life (for the boric acid

electrolyte). Porous anodizing of the aluminum layers was carried out in 0.4 M aqueous solutions of oxalic or tartaric acid.

Anodizing processes were performed at a current density of ~6 mA·cm^{-2} [74,75], except for the reanodizing process, where the current density was manually maintained in the range of 110–530 μA·cm^{-2} due to poor instrumental stabilization at 300 μA·cm^{-2}. Reanodizing was performed through the pores of the anodic alumina, and it is evident that the effective anodizing area was significantly smaller than the area of the experimental sample. These conditions were selected based on extensive investigations on the anodizing of two-layer valve-metal systems.

Chemicals for anodizing were supplied by the Belaquilion additional-liability company and manufactured by Sigma-Aldrich, Inc. (Darmstadt, Germany). A programmable power supply 5751 A (Keysight Technologies Inc., Santa Rosa, CA, USA) was used as the anodizing unit, controlled by a personal computer (PC) with custom software written in LabVIEW 2018 (National Instruments Corp., Austin, TX, USA). Programmable digital multimeters 34,470 A (Keysight Technologies Inc., Santa Rosa, CA, USA) were used to record the voltage-time responses, controlled by a PC with R&D Lab 4.10 "Nanotechnologies" (BSUIR, Minsk, Belarus) developed software. The bulk electrolyte temperature was always set at the beginning of the anodizing process 20 °C with precision ±1 °C without active support during the anodizing process.

The anodizing cell consists of an electrolyte bath with a built-in anode, which is screwed into a base and presses the Gd scrap to the ceramic insert by a PTFE ring. The cathode is made of stainless metal located in the electrolyte. The Gd scrap individually in-traduced in the anodizing cell, were pressed from their face sides by a PTFE ring, so that a circular area of the polish face (Al, Al/Nb) side of the Gd scrap, 63.6 mm^2, was in contact with anodizing solution while the back Gd scrap side was fully isolated from the processing. The anode-to-cathode distance was maintained constant at 5 cm in all experiments. A schematic of a similar electrochemical cell designed for anodizing 100 mm silicon wafers is provided in Ref. [68].

The results presented are representative of at least 3 independent anodizing processes showing similar behaviors.

2.3. Thin Film Characterization

The morphology of the thin films was examined using a scanning electron microscope (SEM) on S-4800 (Hitachi High-Technologies Corp., Tokyo, Japan) operated at an accelerating voltage of 10–15 kV. Prior to imaging, the samples were coated with a 3 nm-thick gold layer by thermal evaporation to mitigate charging effects.

The composition of the anodic thin films was determined by energy-dispersive X-ray spectroscopy (EDX) using a Quantex 200 (Bruker Nano GmbH, Berlin, Germany) with a resolution of 125 eV.

The thin films were examined using a focused ion beam (FIB) on Versa 3D DualBeam (Thermo Fisher Scientific Inc., Waltham, MA, USA) operated at 15 kV.

2.4. Data Processing

Curve-fittings and graphical characteristics were developed using OriginPro 2019 (OriginLab Corp., Northampton, MA, USA).

Free software Fiji 2.17.0 was used to process the results of SEM and FIB.

3. Results and Discussion

3.1. Anodizing Behaviour

3.1.1. Barrier Anodizing of the Gadolinium Scrap in Boric and Citric Acids

Previous studies have indicated that barrier gadolinium oxide can be formed by electrochemical anodizing [62–65]. However, the electrochemical behavior of gadolinium in standard barrier-forming electrolytes—aqueous citric and boric acid solutions—remains poorly understood. This work firstly investigates this unexplored area.

The barrier anodizing processes in aqueous boric and citric acid solutions were conducted without electrolyte stirring. In both cases, vigorous gas bubble evolution was observed at both the anode and the cathode. At the anode, gadolinium undergoes oxidation:

$$2Gd - 6e^{-} \rightarrow 2Gd^{3+} \quad (1)$$

Gd^{3+} ions immediately react with hydroxide ions (OH^{-}), which are formed at the anode surface due to the decomposition of water (see cathodic reactions), or with oxygen from oxo-compounds of acids. The formation of anodic gadolinium oxide proceeds via hydroxide or hydrated oxide intermediates. For simplicity, the overall anodic oxidation process can be represented by the following formal reaction:

$$Gd^{3+} + 3OH^{-} \rightarrow Gd(OH)_3 \quad \text{(intermediate)} \quad (2)$$

$$2Gd(OH)_3 \rightarrow Gd_2O_3 + 3H_2O \quad \text{(field-assisted dehydration)} \quad (3)$$

Formal overall anodic oxidation reaction of Gd can be written as:

$$2Gd + 3H_2O \rightarrow Gd_2O_3 + 6H^{+} + 6e^{-} \quad (4)$$

The process is accompanied by oxygen evolution reaction, as evidenced by the release of gas bubbles:

$$2H_2O - 4^{e-} \rightarrow O_2\uparrow + 4H^{+} \quad (5)$$

An acidic environment, the chelating properties of citric acid, and temperature facilitates the processes of chemical dissolution of metallic gadolinium:

$$2Gd + 6H^{+} \rightarrow 2Gd^{3+} + 3H_2\uparrow \quad (6)$$

In addition to metallic dissolution, chemical etching of the anodic oxide is anticipated. This process is markedly more significant in citric acid than in boric acid. The underlying reason is that Gd^{3+} ions form soluble, stable complexes $[Gd(C_6H_4O_7)]^{+}$ with citrate anions in solution [76]. This complexation effectively removes Gd^{3+} from the oxide precipitation pathway at the surface, thereby promoting etching. In boric acid, the absence of such strong complexing ligands results in a substantially lower chemical dissolution rate of the oxide, favoring its net growth.

Thus, two competing processes occur at the anode: the formation of anodic oxide (Gd_2O_3) and its chemical/electrochemical dissolution. In boric acid, the voltage-current-time (Figure 1a) and the observed film stability indicate that oxide formation is the dominant process. In contrast, the erratic voltage–time response in citric acid (Figure 1b) indicates that dissolution is the dominant process, effectively preventing the formation of a continuous barrier film.

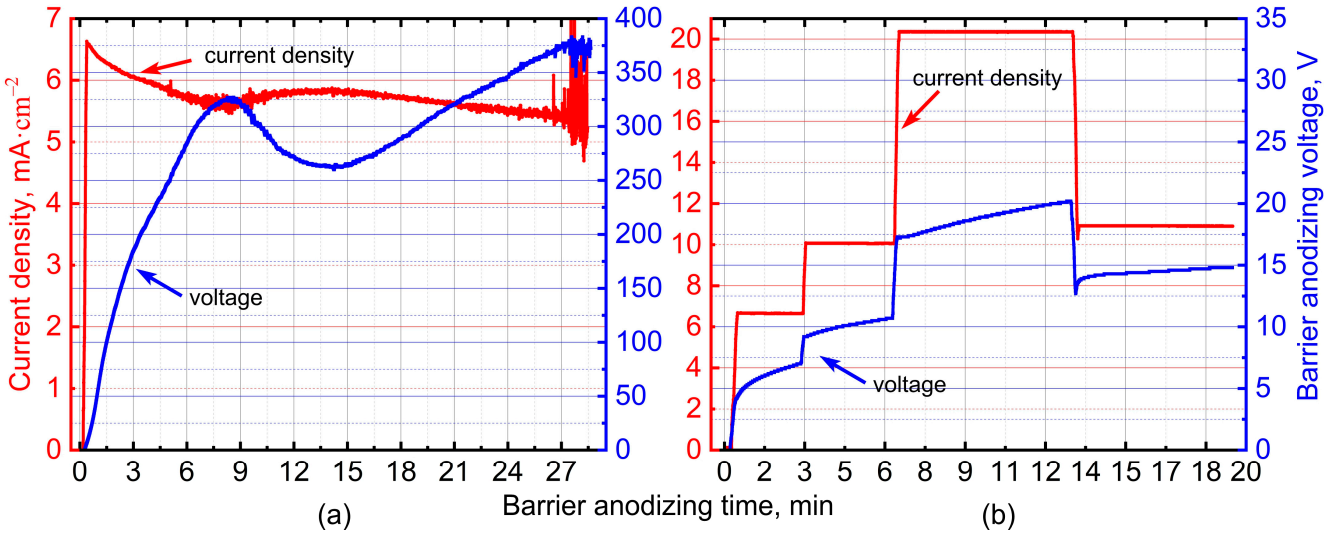

Figure 1. Voltage- and current-time responses during the barrier galvanostatic anodizing in (**a**) 0.5 M H_3BO_3 with 0.05 M $Na_7B_4O_7$ and (**b**) 1% $C_6H_8O_7$ of gadolinium scrap surface.

The initial stage of gadolinium anodizing in boric acid (Figure 1a) exhibits classical behavior: a linear voltage rise under galvanostatic polarization. Minor adjustments to the current density markedly alter the slope of this increase. During this stage, a continuous barrier layer of Gd_2O_3 forms on the pristine metal surface, as described by the overall reaction scheme (Equations (2)–(4)). At a fixed current density, the oxide growth rate—and thus the film thickness—remains constant. Since the voltage is directly proportional to the thickness of this insulating layer, it increases linearly with time. The relatively steep slope indicates that the forming oxide possesses good dielectric properties, effectively resisting current flow and necessitating a higher voltage to sustain the set current. This characteristic response signifies a strong predominance of oxide formation over dissolution.

After approximately 8 min, the growth rate slows and the voltage begins to decline (Figure 1a). This transition is interpreted as follows. Localized heating of the film and adjacent electrolyte, developing over this period, is proposed to accelerate the chemical dissolution of Gd_2O_3. Once dissolution rates surpass oxidation, the net film thickness decreases. By ~13 min, a new dynamic equilibrium is established: the thinner film exhibits lower ionic resistance, which reduces Joule heating and thereby moderates the dissolution rate. Consequently, net oxide growth resumes, leading to a renewed voltage increase with a more gradual slope than in the initial stage.

The altered growth kinetics may also stem from microstructural evolution within the oxide [77]. The initially amorphous Gd_2O_3 can crystallize or hydrate (e.g., to GdOOH) under prolonged anodizing at high voltages (~400 V) [35]. Such phase transformations alter the film's electrical resistivity, changing the voltage required to maintain a constant current. Furthermore, secondary reactions in the boric acid electrolyte may produce other gadolinium species, such as hydroxides, borates, or soluble complexes, adding complexity to the interfacial chemistry.

At approximately 26 min (Figure 1a), the voltage reaches 370 V, and the anodizing process becomes accompanied by significant current and voltage oscillations, along with visible sparking across the entire Gd scrap surface. Although the kinetic curve in Figure 1a shares some features with porous anodizing (such as the voltage plateau followed by a rise), a distinct steady-state region is absent. Direct visual observation confirms that the resulting film possesses a barrier-like morphology.

In contrast to the typical linear voltage–time response observed during barrier anodizing of conventional valve metals, gadolinium exhibits fundamentally different behavior in

citric acid compared to boric acid (Figure 1). A telling distinction is the effect of changing the applied current density. In boric acid (Figure 1a), a decrease in current density from 6 to 5.5 mA·cm^{-2} (decrease by 0.5 mA·cm^{-2}) leads to a noticeable reduction in the slope of the voltage rise. Conversely, in citric acid (Figure 1b), even an increase in current density from 10 to 20 mA·cm^{-2} (increase by 10 mA·cm^{-2}) produces a negligible change in the voltage sweep rate. This pronounced insensitivity indicates that the overall anodic process in citric acid is limited not by oxide growth but by a concurrent chemical reaction—most plausibly, the dissolution of gadolinium or its oxide, which occurs at a rate comparable to the electrochemical oxidation. Elucidating the precise kinetics of this coupled process remains a task for future investigation.

3.1.2. Porous Anodizing of the Al/Gd System in Oxalic Acid

An aqueous oxalic acid solution is an established and effective electrolyte for anodizing Al/Valve-Metal bilayers, known for producing reproducible, well-ordered nanostructures [73,78]. It was selected for the present study due to several advantageous properties relevant to gadolinium anodizing: it is a weak acid (minimizing oxide dissolution), it typically requires lower anodizing voltages than other organic acids, and it is cost-effective, safe, and simple to prepare.

Upon applying a current step to 6 mA·cm^{-2}, the voltage rapidly rises to 45 V (Figure 2a). A subsequent steady-state voltage plateau at ~42.5 V is observed, which is characteristic of stable, ordered porous alumina growth and confirms the good quality of the aluminum layer [74,75]. After approximately 10.5 min, the aluminum is fully consumed, the film becomes visually transparent, and the voltage drops to 37.5 V. The voltage then climbs to a new setpoint of 50 V, at which point the operation switches to potentiostatic mode and the current begins to decay. This current decay may indicate an increase in the overall ionic resistance of the film, potentially due to the onset of gadolinium oxide formation beneath the porous template.

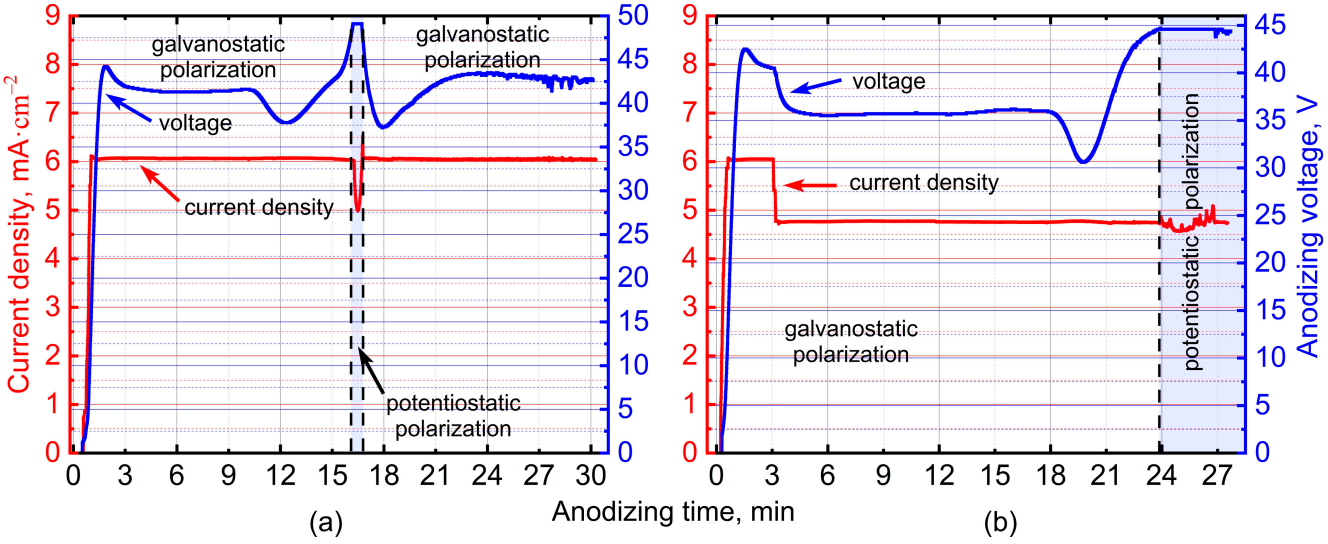

Figure 2. Voltage- and current-time responses during the galvanostatic anodizing in 0.4 M $C_2H_2O_4$ with (**a**) ~6 mA·cm^{-2} and (**b**) ~5 mA·cm^{-2} of Al/Gd systems.

However, after about 1 min in potentiostatic mode, the current begins to rise again while the voltage falls, effectively returning the system to galvanostatic polarization. This reversal indicates a reduction in the film's ionic resistance. The simultaneous visual observation of gas bubble formation and film delamination confirms that dissolution has become the dominant process, leading to structural failure.

Reducing the current density was anticipated to mitigate local Joule heating and, thus, the dissolution rate of the anodic gadolinium oxide. However, as shown in Figure 2b, this expected effect was not realized. After the transition to potentiostatic mode at ~24 min, the current density fails to decrease. Instead, erratic current oscillations commence immediately, and visual inspection reveals gas bubble formation at the interface between the anodic alumina film and the gadolinium substrate. This behavior is attributed to active chemical dissolution of gadolinium (or its oxide) within the confined interlayer region, which disrupts the interface and promotes delamination.

The decay in current density observed after ~16 min of total anodizing time in Figure 2a (following the switch to potentiostatic mode) indicates that oxidation of the underlying gadolinium sublayer has commenced, leading to the initial formation of oxide nanostructures.

3.1.3. Porous Anodizing of the Al/Nb/Gd System in Tartaric Acid

Tartaric acid, another weak organic acid, was selected as the electrolyte for porous anodizing due to its ability to produce anodic alumina with larger cell dimensions compared to oxalic acid. This larger pore-to-pore distance was anticipated to enhance mechanical stability and reduce stress, thereby mitigating the risk of film exfoliation from the gadolinium substrate. To further improve interfacial adhesion and control the subsequent oxidation, a thin niobium interlayer (30 nm) was deposited between the aluminum and gadolinium [79,80]. This niobium layer was intended to act as a barrier, slowing the chemical dissolution of gadolinium oxide and promoting a more controlled growth environment for gadolinium oxide nanostructures.

Porous galvanostatic anodizing was conducted at 6 $mA \cdot cm^{-2}$ with a fast current ramp (Figure 3a). A well-defined steady-state voltage plateau at ~220 V persisted for approximately 8 min, which is characteristic of the stable growth of a cellular-porous anodic alumina structure [74,75]. This plateau voltage is directly related to the pore diameter and cell size of the alumina. To prevent dielectric breakdown, the voltage rise was instrumentally limited to 240 V. Upon reaching this limit, the system switched to potentiostatic operation, and the current density began to drop rapidly.

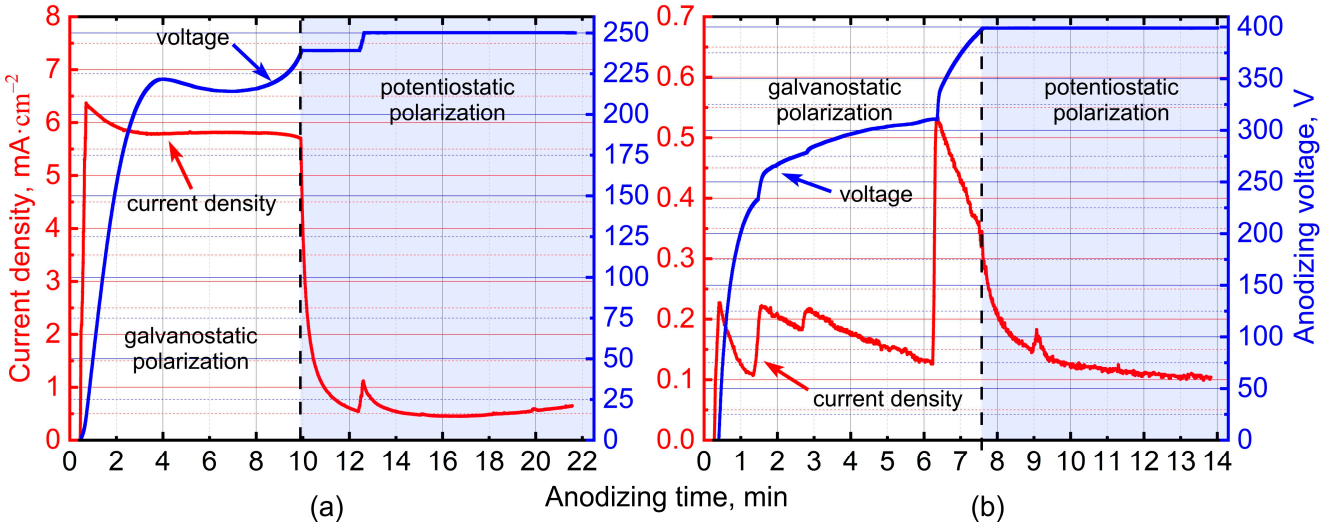

Figure 3. Voltage- and current-time responses during the galvanostatic (**a**) anodizing in 0.4 M $C_4H_6O_6$ and (**b**) reanodizing in 0.5 M H_3PO_4 with 0.05 M $Na_2B_4O_7$ of Al/Nb/Gd systems.

This sharp current decrease is interpreted as the onset of anodic oxidation of the underlying metal layer(s), which possess higher ionic resistivity than alumina. Based on the

established thickness–voltage–current–time responses for anodizing Al/Nb bilayers [68,81], the 30 nm niobium interlayer in the system is fully oxidized by ~150–160 V. Therefore, by the time the voltage plateau ends at ~220 V, the anodizing front has reached the gadolinium substrate. The subsequent slight increase in current density observed after ~16 min (Figure 3a) may be attributed to the dissolution of the newly formed gadolinium oxide, a process consistent with its high chemical activity demonstrated during barrier anodizing (Figure 1).

The voltage–current–time behavior during the galvanostatic reanodizing of the Al/Nb/Gd system is presented in Figure 3b. The initial drop in current density concurrent with the fast voltage rise is attributed to the finite response time of the power supply in galvanostatic mode. Reanodizing commenced at a set current density of ~200 $\mu A \cdot cm^{-2}$. Within the first second, the voltage surged to ~250 V, which was the instrumental limit set during the prior anodizing step. This immediate high voltage indicates that a pre-existing anodic film (comprising Al, Nb, and Gd oxides) with substantial ionic resistance was present, requiring a significant potential to drive current.

After stabilizing at ~250 V for about 1.5 min, the voltage begins a slow, steady increase while the current density is held constant. This voltage rise signifies a progressive increase in the overall ionic resistance of the film. The most plausible explanation for this increase is the continued growth of gadolinium oxide beneath the niobia layer within the alumina pores. The associated Joule heating during this growth phase could locally enhance the dissolution rate of the gadolinium oxide. To counteract this and promote further oxide growth, the applied voltage limit was raised to 400 V at approximately the 6 min mark, effectively increasing the reanodizing rate.

3.2. SEM, FIB and EDX Analysis of Anodic Thin Films

The electrochemical responses presented in Section 3.1 elucidate the anodizing behavior of gadolinium under various configurations (bare metal, and with Al or Al/Nb layers) in different aqueous acid electrolytes. To complement this electrochemical analysis and obtain direct morphology and compositional insight, the resulting anodic films were characterized using SEM, FIB, and EDX (Figure 4).

All SEM images demonstrate the cellular-porous structure characteristic of tartaric acid [74,75]. Analysis of the morphological dimensions of the pores, cells, and thicknesses suggests successful Al anodizing. Figure 4d shows a 32 nm niobium sublayer, which, considering SEM measurement uncertainty, corresponds to the thickness stated in Section 2.1. Several unique and novel features of these films should be highlighted. Figure 4c,d show that the lower portion of the pore is empty, as is the channel in the anodic alumina barrier layer, which was formed during the growth of the anodic niobia nanocolumn [81,82]. The Nb sublayer is absent directly beneath the pore channel and is observed only near the channel entrance. The channel starts at the surface of the gadolinium scrap. A nanocolumn is located in the center of the pore and is not connected to either the film surface or its base. The nanocolumn's height was approximately 340 nm. This configuration, in which the nanocolumn effectively seals the pore opening, is hereafter referred to as the "niobia cork-like effect." A proposed growth mechanism of this structure is discussed in Section 3.3.

To confirm this phenomenon, an additional FIB analysis (Figure 4e) and an investigation of the composition using the EDX analysis (Figure 4f) were carried out. FIB analysis confirmed the existence of niobium cork-like nanocolumns in most alumina pores. The results of the composition analysis are summarized in Table 1.

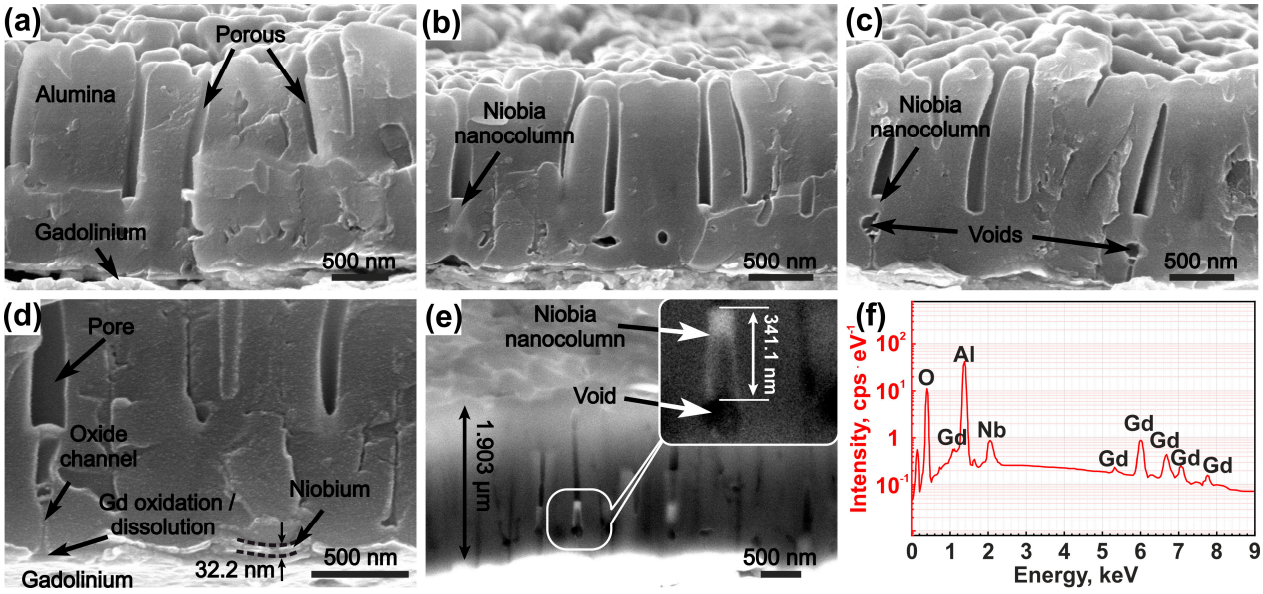

Figure 4. Surface and cross-sectional SEM (**a**–**d**), FIB (**e**) views and EDX (**f**) analysis of anodic thin films made by (**a**) the anodizing of Al(1000 nm)/Nb(30 nm)/Gd(the scrap) systems in 0.4 M $C_4H_6O_6$ at 220 V followed by the reanodizing in 0.5 M H_3PO_4 with 0.05 M $Na_2B_4O_7$ to 400 V, as in Figure 3.

Table 1. EDX point analysis of the anodized and reanodized Al/Nb/Gd systems.

Element	Series	Unn. C [wt.%]	Norm. C [wt.%]	Atom. C [at.%]	Error [wt.%]
Oxygen	K-series	40.17	42.31	58.76	4.5
Aluminum	K-series	45.70	48.14	39.64	2.2
Gadolinium	L-series	6.63	6.99	0.99	0.2
Niobium	L-series	2.43	2.56	0.61	0.1
Total:		94.93	100.00	100.00	

3.3. The Growth Model of Niobia Cork-like Nanocolumns

Based on the electrochemical data (Figures 1–3), the morphological evidence from SEM and FIB (Figure 4a–e), the compositional analysis by EDX (Table 1), and prior knowledge from anodizing similar multilayer systems [82–84], we propose a growth model for the formation of niobia cork-like nanocolumns during the anodizing and reanodizing of Al/Nb/Gd structures.

The initial stages of the proposed model—nucleation, development, and growth of goblet-shaped niobia nanocolumns (Figure 5a–c)—are based on the mechanism established for analogous Al/Nb systems anodized in tartaric acid [82]. Under the applied field, oxygen anions migrate inwards while metal cations migrate outwards, leading to the growth of goblet-like niobia nanocolumns. It is important to note that the subsequent stages illustrated in Figure 5d,e—specifically, the detailed intermixing of oxides and the growth dynamics of the composite nanocolumn—represent a hypothesized extension of the model for the Al/Nb/Gd system. The final stage of the model (Figure 5f), depicting gadolinium oxide dissolution, is consistent with the observed electrochemical response (Figure 3b) and the morphological evidence of a hollow region at the nanocolumn base (Figure 4). However, the detailed mechanisms of ion migration and oxide intermixing proposed farther in the model, while plausible, are inferred from indirect evidence. Direct experimental verification of these specific processes—for example, through in situ spectroscopic or tomographic techniques—represents a clear objective for future research.

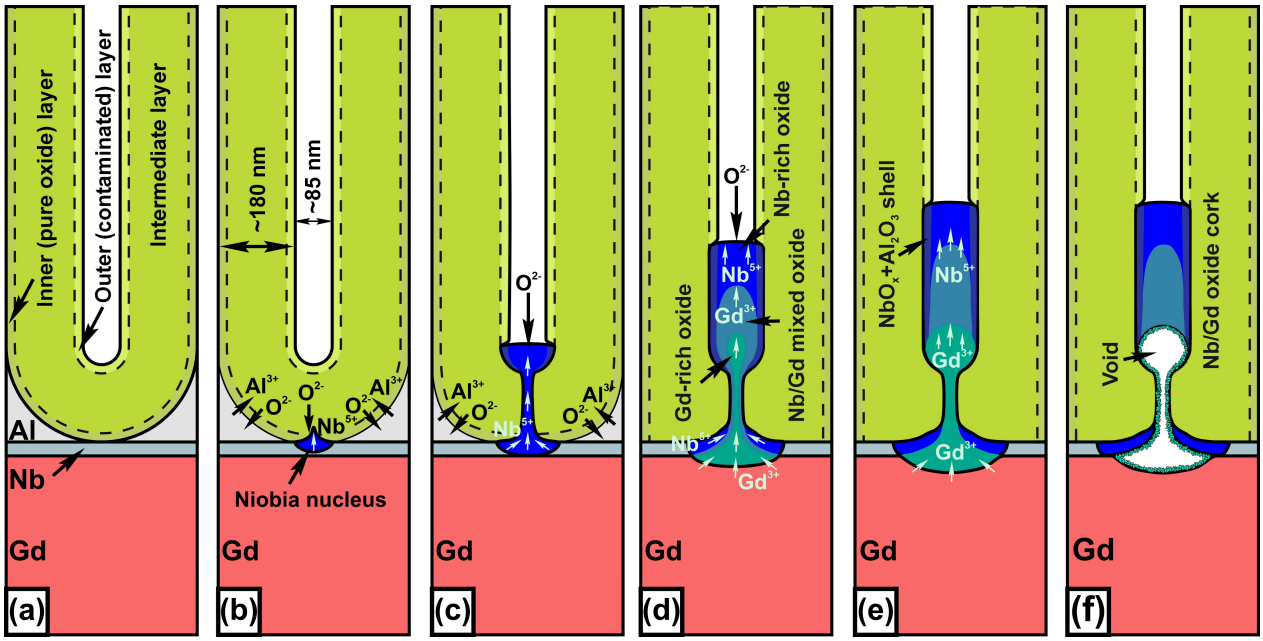

Figure 5. Schematic proposed model of anodic film growth: (**a**) the porous galvanostatic anodizing of aluminum in 0.4 M tartaric acid at ~6 mA·cm^{-2}, (**b**) the beginning of niobium oxidation, (**c**) the end of niobium oxidation, (**d**) the beginning of gadolinium oxidation, (**e**) ~8th min (Figure 3b), reanodizing reaches 400 V and enters potentiostatic mode, (**f**) after ~7.5th min (Figure 3b), dissolution of gadolinium oxide.

Crucially, in the present Al/Nb/Gd system, the 30 nm niobium interlayer is too thin to completely shield the underlying gadolinium from oxidation. Consequently, the anodization of Gd commences even during the later stages of niobium oxidation (evidenced by the current density decay in Figure 3a). Once the anodizing front reaches the Gd substrate, Gd^{3+} cations begin to migrate outwards. As a result, the evolving nanostructure depicted in Figure 5d is not pure niobia but a composite, incorporating gadolinium oxides mixed with niobia and material from the dissolving alumina barrier layer. By the end of the initial anodizing step (Figure 3a), the unconsumed remnants of the Al/Nb bilayer form a continuous network that encapsulates the base of these composite goblet-like nanocolumns (Figure 5d).

During the subsequent reanodizing step (Figure 3b), the residual Al/Nb matrix is progressively consumed, while concurrent oxidation of the Gd substrate leads to the steady upward growth of the composite nanocolumns within the pores (Figure 5e). This creates competition between the consumption of the remaining metal bilayer and the advancement of the gadolinium oxidation front. The large cell size of the anodic alumina template prevents the lateral merger of neighboring oxide bases even at the high reanodizing voltage of 400 V, preserving their isolated, column-like morphology.

We propose that the distinct shell of the goblet-like structure forms via the co-migration of Gd^{3+} and Nb^{5+} cations along the outer, more defective and electrolyte-contaminated regions of the pore walls (e.g., incorporating species like $C_4H_4O_6^{2-}$ from tartaric acid). Concurrent partial dissolution of alumina from the pore wall surfaces [85] accommodates this outward oxide growth. This growth mechanism is active throughout the initial ~7.5 min of reanodizing (Figure 3b). The final height of the nanocolumns, measured from SEM and FIB images, is approximately 600 nm. This is about 100 nm shorter than analogous structures formed in a pure Al/Nb system anodized and reanodized under similar conditions [68,81] a difference potentially attributable to the competing dissolution of gadolinium oxide.

When the reanodizing voltage reaches 400 V at approximately 7.5 min (Figure 3b), the process switches to potentiostatic mode. We hypothesize that this high-voltage plateau may initiate or accelerate the dissolution of gadolinium oxide beneath the niobia "cork" (Figure 5f). The choice of boric acid-based electrolyte for reanodizing appears crucial for this effect. In contrast, the strong complexing and etching nature of citric acid—evident from the barrier anodizing data in Figure 1—prevents the stable formation of such a sealed structure.

The role of boric acid is thus dual and seemingly paradoxical: it facilitates the continued anodic oxidation of the underlying metals while also participating in the chemical dissolution of the gadolinium oxide through or around the niobia plug over extended periods. The precise mechanisms of "cork" formation, the pathways for electrolyte interaction with the sealed interface, and the detailed electrochemical processes occurring beneath it remain unresolved.

4. Conclusions

The methods for preparation of Gd scrap and thin-film systems were developed and investigation of voltage-current-time curves, morphology and composition of anodic thin films on Gd scrap, Al/Gd and Al/Nb/Gd systems in aqueous solutions of citric, boric, oxalic and tartaric acids were carried out. As a result, it was found that:

1. The voltage–time curve of barrier galvanostatic ~6 mA·cm^{-2} anodizing in 0.5 M boric acid solution with the addition of a 0.05 M sodium tetraborate solution is characterized by periods of growth and decline with linear sections: 0–325–263–375 V. The appearance and increase in sparking and oscillations at ~26 min of anodizing is a sign of film degradation.
2. Changing the current density of galvanostatic barrier anodizing of gadolinium scrap in a 1% aqueous solution of citric acid does not have a significant effect on the voltage sweep rate.
3. The voltage–time curve for porous galvanostatic ~6 mA·cm^{-2} and ~5 mA·cm^{-2} anodizing of a two-layer Al/Gd system in a 0.4 M oxalic acid solution exhibits a steady-state region and a region of increasing voltage up to the instrumental limit, characteristic of oxidation of the metallic substrate beneath the pores of the anodic aluminum oxide. However, the subsequent behavior of the voltage-current-time curves is characteristic of film degradation.
4. The voltage–time curve for porous galvanostatic anodizing of a three-layer Al/Nb/Gd system at currents of ~6 mA·cm^{-2} a 0.4 M tartaric acid solution demonstrates a steady-state region and a region of voltage increase up to the instrumental limit, followed by the device's transition to potentiostatic mode and a decrease in current density over a long period of time. This behavior of the voltage-current-time curves is characteristic of oxidation of the metal sublayer through the pores of the anodic alumina.
5. The voltage–time curve of barrier galvanostatic 110–530 μA·cm^{-2} anodizing in 0.5 M boric acid solution with the addition of a 0.05 M sodium tetraborate solution demonstrates a long, smooth increase up to the instrument-limiting voltage 400 V, followed by a transition to potentiostatic mode with a long, smooth decrease in current density. This behavior is typical of the reanodizing process of the valve metal underlayer through the pores of the alumina, accompanied by filling of the pores with anodic oxide.
6. Analysis of the morphology and element composition by SEM, FIB and EDX methods allowed to identify oxide nanocolumns located in the center of the alumina pore and is not connected to either the film surface or its base. The nanocolumn's height was approximately 340 nm. This effect was termed the "Niobia Cork-like Effect" since the oxide nanocolumn resembles a cork that seals the alumina pore.

7. A proposed model of oxide cork growth was developed, including the sequential nucleation, development, growth, mixing of niobium and gadolinium oxides, as well as the process of dissolution of gadolinium oxide in the barrier layer region.

Author Contributions: Conceptualization, methodology, software, project administration, resources, data curation, A.P.; visualization, writing—original draft preparation, writing—review and editing, A.P. and A.L.; investigation, A.P. and S.Z.; formal analysis, validation, A.P., A.L., S.Z. and V.B.; supervision, funding acquisition, V.B. and A.P. All authors have read and agreed to the published version of the manuscript.

Funding: This work was supported by the state program for scientific research of the Republic of Belarus "Convergence 2025" (task 2.2.06.2), "Materials science, new materials and technologies" (task 2.02), "Digital technologies and space informatics" (task 1.10.7.2).

Institutional Review Board Statement: Not Applicable.

Informed Consent Statement: Not Applicable.

Data Availability Statement: The original contributions presented in this study are included in the article. Further inquiries can be directed to the corresponding author.

Acknowledgments: Andrei Pligovka thanks Illia Mashukevich of Belarusian State University of Informatics and Radioelectronics, Minsk, Belarus for the preparation of the 3-D illustrative material.

Conflicts of Interest: The authors declare no conflicts of interest.

References

1. Jorgensen, C.K. Studies on Gadolinium in Geneva since Its Discovery by Marignac in 1880. *Chimia* **1980**, *34*, 381. [CrossRef]
2. Dumazert, J.; Coulon, R.; Lecomte, Q.; Bertrand, G.H.V.; Hamel, M. Gadolinium for Neutron Detection in Current Nuclear Instrumentation Research: A Review. *Nucl. Instrum. Methods Phys. Res. A* **2018**, *882*, 53–68. [CrossRef]
3. Yigitaslan, S.; Erol, K. Chemistry, Physicochemical Properties and Pharmacokinetics of Gadolinium-Based Contrast Agents. In *Medical Imaging Contrast Agents: A Clinical Manual*; Springer: Cham, Switzerland, 2021; pp. 63–69. [CrossRef]
4. Blomqvist, L.K.; Nordberg, G.F.; Aaseth, J. Gadolinium. In *Handbook on the Toxicology of Metals*, 5th ed.; Elsevier: Amsterdam, The Netherlands, 2022; Volume 2, pp. 267–274. [CrossRef]
5. Saini, S.M.; Singh, N.; Nautiyal, T.; Auluck, S. Optical and Magneto-Optical Properties of Gadolinium. *J. Appl. Phys.* **2007**, *101*, 033523. [CrossRef]
6. Chen, J.; Zhang, X.; Xiao, W.; Pan, D.; Wu, W. Advances in Gadolinium-Based Composite Materials for Neutron and Gamma-Ray Shielding. *Front. Mater.* **2025**, *12*, 1561198. [CrossRef]
7. Laing, M. Gadolinium: Central Metal of the Lanthanoids. *J. Chem. Educ.* **2009**, *86*, 188–189. [CrossRef]
8. Li, J.; Mao, N.; Zhang, X.; Wang, S.; Yang, F.; Lu, W.; Yang, H.; Yang, W.; Zhang, L.; Wu, D.; et al. Effect of Gadolinium Addition on Microstructure, Mechanical Properties and Corrosion Behavior of Titanium Alloys for Spent Fuel Storage and Neutron Shielding. *J. Rare Earths* **2025**, *43*, 1996–2004. [CrossRef]
9. Nicodemo, G.; Zullo, G.; Cappia, F.; Van Uffelen, P.; De Lara, A.; Luzzi, L.; Pizzocri, D. Chromia-Doped UO2 Fuel: An Engineering Model for Chromium Solubility and Fission Gas Diffusivity. *J. Nucl. Mater.* **2024**, *601*, 155301. [CrossRef]
10. Safavi, S.M.; Outokesh, M.; Vosoughi, N.; Yahyazadeh, A.; Mohammadi, A.; Kiani, M.A.; Jabalamelian, S.S. Preparation and Characterization of a New Gd_2O_3-Epoxy Composite for Neutron Shielding Applications. *Sci. Rep.* **2024**, *14*, 25663. [CrossRef] [PubMed]
11. Wang, K.; Ma, L.; Yang, C.; Bian, Z.; Zhang, D.; Cui, S.; Wang, M.; Chen, Z.; Li, X. Recent Progress in Gd-Containing Materials for Neutron Shielding Applications: A Review. *Materials* **2023**, *16*, 4305. [CrossRef]
12. Shayakubova, Y. Design and Development of a Neutron Collimator. *arXiv* **2021**, arXiv:2108.03238.
13. Barreca, D.; Gasparotto, A.; Milanov, A.; Tondello, E.; Devi, A.; Fischer, R.A. Gd_2O_3 Nanostructured Thin Films Analyzed by XPS. *Surf. Sci. Spectra* **2007**, *14*, 60–67. [CrossRef]
14. Li, Y.L.; Chen, N.F.; Zhou, J.P.; Song, S.L.; Liu, L.F.; Yin, Z.G.; Cai, C.L. Effect of the Oxygen Concentration on the Properties of Gd2O3 Thin Films. *J. Cryst. Growth* **2004**, *265*, 548–552. [CrossRef]
15. Lay, T.S.; Liao, Y.Y.; Hung, W.H.; Hong, M.; Kwo, J.; Mannaerts, J.P. Depth-Profile Study of the Electronic Structures at $Ga_2O_3(Gd_2O_3)$ and Gd_2O_3–GaN Interfaces by X-Ray Photoelectron Spectroscopy. *J. Cryst. Growth* **2005**, *278*, 624–628. [CrossRef]

16. Yorulmaz, N.; Yasar, M.M.; Acikgoz, A.; Kavun, Y.; Demircan, G.; Kamislioglu, M.; Aktas, B.; Ulas, E.O. Influence of Gd_2O_3 on Structural, Optical, Radiation Shielding, and Mechanical Properties of Borate Glasses. *Opt. Mater.* **2024**, *149*, 115032. [CrossRef]
17. Kuznetsova, Y.A.; Zatsepin, A.F.; Gavrilov, N.V. The High Refractive Index of Gd_2O_3 Thin Films Obtained by Magnetron Sputtering. *Opt. Mater.* **2021**, *120*, 111382. [CrossRef]
18. Leighly, K.M.; Choi, H. Enhancement of Photoluminescence Emission of Gd^{3+} Activated Borate Phosphors for Phototherapy Lamps: A Review. *J. Phys. Conf. Ser.* **2021**, *1913*, 012031. [CrossRef]
19. Misiak, M.; Pavlosiuk, O.; Szalkowski, M.; Kotulska, A.; Ledwa, K.; Bednarkiewicz, A. On the Role of Gd^{3+} Ions in Enhancement of UV Emission from Yb^{3+}–Tm^{3+} up-Converting LiYF4 Nanocrystals. *Nanotechnology* **2023**, *34*, 345702. [CrossRef]
20. Priya, R.; Pandey, O.P.; Dhoble, S.J. Review on the Synthesis, Structural and Photo-Physical Properties of Gd_2O_3 Phosphors for Various Luminescent Applications. *Opt. Laser Technol.* **2021**, *135*, 106663. [CrossRef]
21. Wang, X.; Zhang, P.; Wang, F.; Liu, S.; Tian, Y.; Yang, B. Highly Enhanced Luminescence of Gd_2O_3:Ho^{3+} Phosphor by Heat Treatment. *Mater. Chem. Phys.* **2023**, *306*, 127985. [CrossRef]
22. Tamrakar, R.K.; Upadhyay, K.; Tamrakar, R.K.; Upadhyay, K. Gd_2O_3: A Luminescent Material. In *Rare Earth Elements and Their Minerals*; IntechOpen: London, UK, 2020. [CrossRef]
23. Sun, J.; Du, Y.; Luo, Z.; Guo, H.; Liu, Y.; Sun, P.; Jiang, J. Enhanced X-Ray Imaging with Gd_2O_2S:Pr-Epoxy Composite Films: Synthesis, High-Resolution Performance, and Flexibility. *ACS Appl. Electron. Mater.* **2024**, *6*, 2782–2787. [CrossRef]
24. De Martinis, A.; Montalto, L.; Scalise, L.; Rinaldi, D.; Mengucci, P.; Michail, C.; Fountos, G.; Martini, N.; Koukou, V.; Valais, I.; et al. Luminescence and Structural Characterization of Gd_2O_2S Scintillators Doped with Tb^{3+}, Ce^{3+}, Pr^{3+} and F for Imaging Applications. *Crystals* **2022**, *12*, 854. [CrossRef]
25. Ma, Y.; Xin, M.; Li, Z.; Guan, Y. Study on Photocurable Printing and Luminescence Properties of Gd_2O_3:Eu^{3+} Ceramics. *J. Alloys Compd.* **2025**, *1039*, 183185. [CrossRef]
26. Wang, Y.; Milosevic, O.; Gomez, L.; Rabanal, M.E.; Torralba, J.M.; Yang, B.; Townsend, P.D. Thermoluminescence Responses from Europium Doped Gadolinium Oxide. *J. Phys. Condens. Matter* **2006**, *18*, 9257. [CrossRef]
27. Zhang, K.; Dondapati, H.; Holloway, T.; Cao, W.; Kar, A.; Patra, A.; Pradhan, A.K. Influence of Morphological Transformation on Luminescence Properties of Europium-Doped Gadolinium Oxide Nanostructures. *J. Nanophotonics* **2010**, *4*, 043517. [CrossRef]
28. Nadeera Hemamali, G.M.; Smith, D.R.; Hobson, P.R.; Fern, G.; Ireland, T. Europium Doped Gd_2O_3 and $GdBO_3$ Scintillators for Thermal Neutron Detection. *Nucl. Instrum. Methods Phys. Res. A* **2023**, *1048*, 167918. [CrossRef]
29. Cha, B.K.; Lee, S.J.; Muralidharan, P.; Kim, J.Y.; Kim, D.K.; Lee, D.H.; Yun, J.Y.; Cho, G. Synthesis and Scintillation Properties of Nano Gd_2O_3(Eu) Scintillator for High Resolution X-Ray Imaging Applications. *Nucl. Instrum. Methods Phys. Res. A* **2010**, *619*, 174–176. [CrossRef]
30. Hsu, K.-S.; Yang, C.-F.; Nancy, A.; Souza, D.'; Sayyed, M.I.; Kamath, S.D. Impact of Gd_2O_3 Incorporation in Structural, Optical, Thermal, Mechanical, and Radiation Blocking Nature in HMO Boro-Tellurite Glasses. *Eng. Proc.* **2024**, *55*, 97. [CrossRef]
31. Intachai, N.; Wantana, N.; Kaewjaeng, S.; Chaiphaksa, W.; Cheewasukhanont, W.; Htun, K.T.; Kothan, S.; Kim, H.J.; Kaewkhao, J. Effect of Gd_2O_3 on Radiation Shielding, Physical and Optical Properties of Sodium Borosilicate Glass System. *Radiat. Phys. Chem.* **2022**, *199*, 110361. [CrossRef]
32. Li, J.; Chen, B.; Li, Y.; Li, B.; Huang, F.; Lei, R.; Xu, S. Mid-Infrared Luminescence of Gd_2O_3-Based Nano-Glass Ceramic with Remarkable Stability. *Ceram. Int.* **2021**, *47*, 32407–32413. [CrossRef]
33. Reddy, N.M.; Reddy, N.M. Effect of Rare Earth Ions Doping on Glass Materials. In *Glass Science-Innovations and Applications*; IntechOpen: London, UK, 2025. [CrossRef]
34. Gao, P.H.; Zeng, S.C.; Jin, C.; Zhang, B.; Chen, B.Y.; Yang, Z.; Guo, Y.C.; Liang, M.X.; Li, J.P.; Li, Q.P.; et al. Effect of Gd_2O_3 Addition on the Microstructure and Properties of Gd_2O_3-Yb_2O_3-Y_2O_3-ZrO_2 (GYYZO) Ceramics. *Materials* **2021**, *14*, 7470. [CrossRef]
35. Jamnezhad, H.; Jafari, M. Structure of Gd_2O_3 Nanoparticles at High Temperature. *J. Magn. Magn. Mater.* **2016**, *408*, 164–167. [CrossRef]
36. Berki, T.R.; Martinelli, J.; Tei, L.; Willcock, H.; Butler, S.J. Polymerizable Gd(III) Building Blocks for the Synthesis of High Relaxivity Macromolecular MRI Contrast Agents. *Chem. Sci.* **2021**, *12*, 3999–4013. [CrossRef]
37. Li, Q.; Chen, J.; Zhang, X.; Ruan, C.; Wu, W. Hydrophilic Modification of Gadolinium Oxide by Building Double Molecular Structures. *Nanomaterials* **2025**, *15*, 1421. [CrossRef]
38. Ahab, A.; Rohman, F.; Iskandar, F.; Haryanto, F.; Arif, I. A Simple Straightforward Thermal Decomposition Synthesis of PEG-Covered Gd_2O_3 (Gd_2O_3@PEG) Nanoparticles. *Adv. Powder Technol.* **2016**, *27*, 1800–1805. [CrossRef]
39. Palewski, T.; Tristan, N.V.; Drulis, H.; Ćwik, J. Hydrogenation Process of the Gd3M (M = Ni or Co) Intermetallics Compound. *J. Alloys Compd.* **2005**, *404–406*, 584–587. [CrossRef]
40. Barzilai, S.; Mintz, M.H. The Effects of Vacancies and Surface Hydroxyls on the Interactions of Hydrogen with Rare Earth Oxides—DFT Calculations on Gadolinium Oxide. *J. Alloys Compd.* **2018**, *740*, 926–934. [CrossRef]

41. Christian Raja, A.A.; Sinthiya, A.S.I.J.; Selvam, V.; Anitha, C.; Malathi, B. Fabrication of Gd_2O_3-Loaded Nitrogen-Rich C_3N_5@PANI Hybrid Nanocomposites: Unlocking Efficient Photocatalysis for Long-Term Organic Dye Degradation in Wastewater Treatment. *Phys. B Condens. Matter* **2025**, *698*, 416758. [CrossRef]
42. Wu, K.; Zanina, A.; Kondratenko, V.A.; Xu, L.; Li, J.; Chen, J.; Lund, H.; Bartling, S.; Li, Y.; Jiang, G.; et al. Fundamentals of Unanticipated Efficiency of Gd_2O_3-Based Catalysts in Oxidative Coupling of Methane. *Angew. Chem. Int. Ed.* **2024**, *63*, e202319192. [CrossRef]
43. Urazov, K.K.; Sviridenko, N.N.; Sviridenko, Y.A.; Utyaganova, V.R. Influence of a Precursor Catalyst on the Composition of Products in Catalytic Cracking of Heavy Oil. *Energies* **2024**, *17*, 2016. [CrossRef]
44. Alreshaidan, S.B.; Al-Fatesh, A.; Lanre, M.S.; Alanazi, Y.M.; Ibrahim, A.A.; Fakeeha, A.H.; Albaqi, F.; Anojaidi, K.; Bagabas, A. Effect of Adding Gadolinium Oxide Promoter on Nickel Catalyst over Yttrium-Zirconium Oxide Support for Dry Reforming of Methane. *Materials* **2023**, *16*, 1158. [CrossRef] [PubMed]
45. Garg, A.B.; Muñoz, A.; Anzellini, S.; Sánchez-Martín, J.; Turnbull, R.; Díaz-Anichtchenko, D.; Popescu, C.; Errandonea, D. Role of GdO Addition in the Structural Stability of Cubic Gd_2O_3 at High Pressures: Determination of the Equation of States of GdO and Gd_2O_3. *Materialia* **2024**, *34*, 102064. [CrossRef]
46. Das, S.; Bhaskar, R.; Narayanan, K.B. Multifunctional Applications of Gadolinium-Doped Cerium Oxide ($Ce_{1-X}Gd_xO_{2-\partial}$) Ceramics: A Review. *J. Rare Earths* **2024**, *42*, 1817–1834. [CrossRef]
47. Wu, J.; Wang, H.; Xu, J.; Liu, Y.; Feng, X.; Fan, F.; Wang, X.; Gao, F. Enhanced Thermophysical and Mechanical Properties of Gadolinium Zirconate Ceramics via Non-Stoichiometric Design. *J. Eur. Ceram. Soc.* **2024**, *44*, 116790. [CrossRef]
48. Sarikhani, A.; Alamzadeh, Z.; Beik, J.; Irajirad, R.; Mirrahimi, M.; Pirhajati Mahabadi, V.; Kamrava, S.K.; Ghaznavi, H.; Khoei, S. Ultrasmall Fe_3O_4 and Gd_2O_3 Hybrid Nanoparticles for T_1-Weighted MR Imaging of Cancer. *Cancer Nanotechnol.* **2022**, *13*, 43. [CrossRef]
49. Yue, H.; Marasini, S.; Ahmad, M.Y.; Ho, S.L.; Cha, H.; Liu, S.; Jang, Y.J.; Tegafaw, T.; Ghazanfari, A.; Miao, X.; et al. Carbon-Coated Ultrasmall Gadolinium Oxide (Gd_2O_3@C) Nanoparticles: Application to Magnetic Resonance Imaging and Fluorescence Properties. *Colloids Surf. A Physicochem. Eng. Asp.* **2020**, *586*, 124261. [CrossRef]
50. Mortezazadeh, T.; Gholibegloo, E.; Riyahi, A.N.; Haghgoo, S.; Musa, A.E.; Khoobi, M. Glucosamine Conjugated Gadolinium (III) Oxide Nanoparticles as a Novel Targeted Contrast Agent for Cancer Diagnosis in MRI. *J. Biomed. Phys. Eng.* **2020**, *10*, 25. [CrossRef]
51. Mulugeta, E.; Tegafaw, T.; Liu, Y.; Zhao, D.; Chen, X.; Baek, A.; Kim, J.; Chang, Y.; Lee, G.H. Current Status and Future Aspects of Gadolinium Oxide Nanoparticles as Positive Magnetic Resonance Imaging Contrast Agents. *Nanomaterials* **2025**, *15*, 1340. [CrossRef]
52. Boopathi, G.; Raj, S.G.; Kumar, G.R.; Mohan, R. Co-Precipitation Synthesis, Structural and Luminescent Behavior of Erbium Doped Gadolinium Oxide (Er^{3+}:Gd_2O_3) Nanorods. *Procedia Mater. Sci.* **2014**, *6*, 1436–1443. [CrossRef]
53. Selvaraju, C.; Karthick, R.; Veerasubam, R. The Modification of Structural, Optical and Antibacterial Activity Properties of Rare Earth Gadolinium-Doped ZnO Nanoparticles Prepared by Co-Precipitation Method. *J. Inorg. Organomet. Polym. Mater.* **2019**, *29*, 776–782. [CrossRef]
54. Niftaliev, S.I.; Kuznetsova, I.V.; Saranov, I.A.; Zhundrikova, T.V.; Lygina, L.V.; Tuneekov, V.Y.; Chislova, I.V.; Zvereva, I.A. Synthesis of Nanosized Gadolinium Oxide. *Glass Phys. Chem.* **2019**, *45*, 232–237. [CrossRef]
55. Bakovets, V.V.; Trushnikova, L.N.; Plyusnin, P.E.; Korolkov, I.V.; Dolgovesova, I.P.; Pivovarova, T.D.; Savintseva, S.A. Features of the Sol-Gel Process of Formation of Nanostructured Gadolinium Oxide. *Russ. J. Gen. Chem.* **2013**, *83*, 1808–1814. [CrossRef]
56. Simoneti, J.A.; Davolos, M.R.; Jafelicci, M. Hydrothermal Treatment of Gadolinium Oxide in Presence of Silica. *Int. J. High Press. Res.* **1994**, *12*, 353–360. [CrossRef]
57. Hemmer, E.; Kohl, Y.; Mathur, S.; Thielecke, H.; Soga, K. Solvothermal Synthesis of Gadolinium Hydroxide and Oxide Powders and Their Potential for Biomedical Applications. *Ceram. Trans.* **2010**, *214*, 27–37. [CrossRef]
58. Wang, Y.; Bai, X.; Liu, T.; Dong, B.; Xu, L.; Liu, Q.; Song, H. Solvothermal Synthesis and Luminescence Properties of Monodisperse Gd_2O_3:Eu^{3+} and Gd_2O_3:Eu^{3+}@SiO_2 Nanospheres. *J. Solid State Chem.* **2010**, *183*, 2779–2785. [CrossRef]
59. Tarasenko, N.V.; Butsen, A.V.; Nevar, A.A. Laser Ablation of Gadolinium Targets in Liquids for Nanoparticle Preparation. *Appl. Phys. A Mater. Sci. Process.* **2008**, *93*, 837–841. [CrossRef]
60. Cheng, X.; Xu, D.; Song, Z.; He, D.; Yu, Y.; Zhao, Q.; Shen, D.S. Characterization of Gadolinium Oxide Film by Pulse Laser Deposition. *Appl. Surf. Sci.* **2009**, *256*, 921–923. [CrossRef]
61. Grave, D.A.; Hughes, Z.R.; Robinson, J.A.; Medill, T.P.; Hollander, M.J.; Stump, A.L.; Labella, M.; Weng, X.; Wolfe, D.E. Process–Structure–Property Relations of Micron Thick Gd_2O_3 Films Deposited by Reactive Electron-Beam Physical Vapor Deposition (EB-PVD). *Surf. Coat. Technol.* **2012**, *206*, 3094–3103. [CrossRef]
62. NISHIKAWA, H.; MINAMI, S. The Anodic Oxidation of Gadolinium. *J. Met. Finish. Soc. Jpn.* **1982**, *33*, 391–393. [CrossRef]
63. Gruss, L.; Mackus, T. The Anodization of Several Rare Earth Metals in Sodium Silicate Solutions. *J. Electrochem. Soc.* **1974**, *121*, 1402. [CrossRef]

64. Kuei, P.Y.; Hu, C.C. Gadolinium Oxide *High-k* Gate Dielectrics Prepared by Anodic Oxidation. *Appl. Surf. Sci.* **2008**, *254*, 5487–5491. [CrossRef]
65. Pan, T.M.; Liao, C.S.; Hsu, H.H.; Chen, C.L.; Der Lee, J.; Wang, K.T.; Wang, J.C. Excellent Frequency Dispersion of Thin Gadolinium Oxide *High-k* Gate Dielectrics. *Appl. Phys. Lett.* **2005**, *87*, 262908. [CrossRef]
66. Mozalev, A.M.; Plihauka, A.N.; Luferov, A.N.; Popichev, E.L. High Frequency Characteristics of MIM Capacitors with Nanostructured Anodic Oxide Dielectrics. In Proceedings of the KpbiMuKo 2009 CriMiCo—2009 19th International Crimean Conference Microwave and Telecommunication Technology, Sevastopol, Ukraine, 14–18 September 2009.
67. Ghorbanhossaini, A.; Rafiee, R.; Pligovka, A.; Salerno, M. Dental Composites with Strength after Aging Improved by Using Anodic Nanoporous Fillers: Experimental Results, Modeling, and Simulations. *Eng. Comput.* **2023**, *39*, 387–398. [CrossRef]
68. Pligovka, A.; Lazavenka, A.; Gorokh, G. Anodic Niobia Column-like 3-D Nanostructures for Semiconductor Devices. *IEEE Trans. Nanotechnol.* **2019**, *18*, 790–797. [CrossRef]
69. Ottone, C.; Laurenti, M.; Bejtka, K.; Sanginario, A.; Cauda, V. The Effects of the Film Thickness and Roughness in the Anodization Process of Very Thin Aluminum Films. *J. Mater. Sci. Nanotechnol.* **2014**, *1*, 1. [CrossRef]
70. Lebyedyeva, T.; Kryvyi, S.; Lytvyn, P.; Skoryk, M.; Shpylovyy, P. Formation of Nanoporous Anodic Alumina by Anodization of Aluminum Films on Glass Substrates. *Nanoscale Res. Lett.* **2016**, *11*, 203. [CrossRef] [PubMed]
71. Pligovka, A. Reflectant Photonic Crystals Produced via Porous-Alumina-Assisted-Anodizing of Al/Nb and Al/Ta Systems. *Surf. Rev. Lett.* **2021**, *2150055*. [CrossRef]
72. Mozalev, A.; Gorokh, G.; Sakairi, M.; Takahashi, H. The Growth and Electrical Transport Properties of Self-Organized Metal/Oxide Nanostructures Formed by Anodizing Ta-Al Thin-Film Bilayers. *J. Mater. Sci.* **2005**, *40*, 6399–6407. [CrossRef]
73. Pligovka, A.; Zakhlebayeva, A.; Lazavenka, A. Niobium Oxide Nanocolumns Formed via Anodic Alumina with Modulated Pore Diameters. *J. Phys.: Conf. Ser.* **2018**, *987*, 012006. [CrossRef]
74. Roslyakov, I.V.; Gordeeva, E.O.; Napolskii, K.S. Role of Electrode Reaction Kinetics in Self-Ordering of Porous Anodic Alumina. *Electrochim. Acta* **2017**, *241*, 362–369. [CrossRef]
75. Bu, S.D.; Choi, Y.C.; Hyeon, J.Y.; Bae, T.S. Effects of Anodizing Voltages on the Pore Morphology Formation of Porous Anodic Aluminas and Corresponding Current Density Variations. *J. Korean Phys. Soc.* **2009**, *55*, 835–840. [CrossRef]
76. Ivanova, V.Y.; Shurygin, I.D.; Chevela, V.V.; Ajsuvakova, O.P.; Semenov, V.E.; Bezryadin, S.G. New Aspects of Complex Formation in the Gadolinium(III)–Citric Acid System in Aqueous Solution. *Comments Inorg. Chem.* **2022**, *42*, 109–144. [CrossRef]
77. Whba, F.; Mohamed, F.; Md Rosli, N.R.A.; Abdul Rahman, I.; Idris, M.I. The Crystalline Structure of Gadolinium Oxide Nanoparticles (Gd_2O_3-NPs) Synthesized at Different Temperatures via X-Ray Diffraction (XRD) Technique. *Radiat. Phys. Chem.* **2021**, *179*, 109212. [CrossRef]
78. Pligovka, A.; Hoha, A.; Turavets, U.; Poznyak, A.; Zakharau, Y. Formation Features, Morphology and Optical Properties of Nanostructures via Anodizing Al/Nb on Si and Glass. *Mater. Today Proc.* **2021**, *37*, A8–A15. [CrossRef]
79. Song, G.; Remhof, A.; Theis-Bröhl, K.; Zabel, H. Extraordinary Adhesion of Niobium on Sapphire Substrates. *Phys. Rev. Lett.* **1997**, *79*, 5062. [CrossRef]
80. Strunk, C.; Sürgers, C.; Paschen, U.; Löhneysen, H.V. Superconductivity in Layered Nb/Gd Films. *Phys. Rev. B* **1994**, *49*, 4053. [CrossRef]
81. Gorokh, G.G.; Pligovka, A.N.N.; Lozovenko, A.A.A. Columnar Niobium Oxide Nanostructures: Mechanism of Formation, Microstructure, and Electrophysical Properties. *Tech. Phys.* **2019**, *64*, 1657–1665. [CrossRef]
82. Mozalev, A.; Sakairi, M.; Saeki, I.; Takahashi, H. Nucleation and Growth of the Nanostructured Anodic Oxides on Tantalum and Niobium under the Porous Alumina Film. *Electrochim. Acta* **2003**, *48*, 3155–3170. [CrossRef]
83. Hoha, A.; Poznyak, A.; Pligovka, A. Porous Alumina Assisted Anodizing of Ti/Nb Layers. In Proceedings of the 2024 IEEE 24th International Conference on Nanotechnology (NANO), Gijon, Spain, 8–11 July 2024; pp. 570–573. [CrossRef]
84. Mozalev, A.; Bendova, M.; Kalina, L.; Prasek, J.; Gispert-Guirado, F.; Llobet, E. MoOx-Based High-Density Nanoarrays on a Substrate via Smart Anodizing as Novel 3D Electrodes for Nano-Energy Applications. *J. Mater. Chem. A Mater.* **2025**, *13*, 19605–19622. [CrossRef]
85. Zhukovskyy, V.; Zhukovska, N.; Hrabovskyi, D. About Modeling Intraparticle Diffusion in Porous Catalysts Using Fractional Differential Equations. In Proceedings of the 2025 15th International Conference on Advanced Computer Information Technologies (ACIT), Sibenik, Croatia, 17–19 September 2025; pp. 206–211. [CrossRef]

Disclaimer/Publisher's Note: The statements, opinions and data contained in all publications are solely those of the individual author(s) and contributor(s) and not of MDPI and/or the editor(s). MDPI and/or the editor(s) disclaim responsibility for any injury to people or property resulting from any ideas, methods, instructions or products referred to in the content.